The Astrophysical Journal Letters, 937:L38 (11pp), 2022 October 1 https://doi.org/10.3847/2041-8213/ac92e2

Explanation of Heliospheric Energetic Neutral Atom Fluxes Observed by the Interstellar Boundary Explorer

E. J. Zirnstein[1], T. K. Kim[2], M. A. Dayeh[3,4], J. S. Rankin[1], D. J. McComas[1], and P. Swaczyna[1]
[1] Department of Astrophysical Sciences, Princeton University, Princeton, NJ 08544, USA; ejz@princeton.edu
[2] Center for Space Plasma and Aeronomic Research, University of Alabama in Huntsville, Huntsville, AL 35805, USA
[3] Southwest Research Institute, San Antonio, TX 78228, USA
[4] Department of Physics and Astronomy, University of Texas at San Antonio, San Antonio, TX 78249, USA
Received 2022 July 19; revised 2022 August 30; accepted 2022 September 19; published 2022 September 30

Abstract

Interstellar neutral atoms propagating into the heliosphere experience charge exchange with the supersonic solar wind (SW) plasma, generating ions that are picked up by the SW. These pickup ions (PUIs) constitute ∼25% of the proton number density by the time they reach the heliospheric termination shock (HTS). Preferential acceleration of PUIs at the HTS leads to a suprathermal, kappa-like PUI distribution in the heliosheath, which may be further heated in the heliosheath by traveling shocks or pressure waves. In this study, we utilize a dynamic, 3D magnetohydrodynamic model of the heliosphere to show that dynamic heating of PUIs at the HTS and in the inner heliosheath (IHS), as well as a background source of energetic neutral atoms (ENAs) from outside the heliopause, can explain the heliospheric ENA signal observed by the Interstellar Boundary Explorer (IBEX) in the Voyager 2 direction. We show that the PUI heating process at the HTS is characterized by a polytropic index larger than 5/3, likely ranging between $\gamma \sim 2.3$ and 2.7, depending on the time in solar cycle 24 and SW conditions. The ENA fluxes at energies >1.5 keV show large-scale behavior in time with the solar cycle and SW dynamic pressure, whereas ENAs < 1.5 keV primarily exhibit random-like fluctuations associated with SW transients affecting the IHS. We find that $\lesssim$20% of the ENAs observed at ∼0.5–6 keV come from other sources, likely from outside the heliopause as secondary ENAs. This study offers the first model replication of the intensity and evolution of IBEX-Hi ENA observations from the outer heliosphere.

Unified Astronomy Thesaurus concepts: Pickup ions (1239); Termination shock (1690); Heliosphere (711); Heliosheath (710); Ion-neutral reactions (2263); Interstellar medium (847); Interplanetary particle acceleration (826)

1. Introduction

The heliosphere's interaction with the local interstellar medium (LISM; Parker 1961) is significantly mediated by the presence of interstellar neutral atoms that transfer mass, momentum, and energy via photoionization, electron impact ionization, and charge exchange processes (Baranov & Malama 1993; Bzowski et al. 2013). The ionization of interstellar neutrals results in the creation of nonthermal pickup ions (PUIs) in the solar wind (SW). While it was generally assumed that PUIs adiabatically cool with distance from the Sun, defined by an adiabatic index of $\alpha = 3/2$, New Horizons' Solar Wind Around Pluto (SWAP) observations have revealed that the majority of PUIs exhibit additional heating ($\alpha > 3/2$) out to at least ∼47 au from the Sun (McComas et al. 2021). These authors further showed that PUIs constitute ∼12% of the proton number density halfway to the heliospheric termination shock (HTS), already dominating the internal plasma pressure, and predict that PUIs will reach ∼25% of the proton density at the HTS.

The PUIs are preferentially accelerated at the HTS compared to SW ions (SWIs) due to their ability for reflection at the shock magnetic barrier and cross-shock potential (Zank et al. 1996; Yang et al. 2015; Kumar et al. 2018; Giacalone et al. 2021; Zirnstein et al. 2021b). While so far, there have been no direct observations of PUIs at the HTS, SWAP observations revealed the first direct measurement of preferential PUI heating at interplanetary shocks in the outer heliosphere (Zirnstein et al. 2018b). Recent SWAP observations achieved at significantly higher cadence than ever before show that progressively higher PUI heating occurs with stronger shock compression ratios (McComas et al. 2022).

Downstream of the HTS, PUIs advect with the bulk plasma in the inner heliosheath (IHS) as it flows through and then diverts back tailward inside the heliopause boundary. Some PUIs produce energetic neutral atoms (ENAs) with Earth-bound trajectories that can be detected by the Interstellar Boundary Explorer (IBEX). IBEX all-sky observations of ENAs over ∼0.5–6 keV reveal a "globally distributed flux" (GDF) across the sky, as well as a narrower "ribbon" of ENAs originating from outside the heliopause (McComas et al. 2009). The GDF, believed to primarily originate from the IHS, exhibits power law–like spectra (Zirnstein et al. 2021a). However, thus far, the total intensity of the observed GDF has proven challenging to recreate in models (Zirnstein et al. 2017; Baliukin et al. 2020; Fuselier et al. 2021; Kornbleuth et al. 2021; Gkioulidou et al. 2022), suggesting the importance of turbulence at the HTS (Giacalone et al. 2021; Zirnstein et al. 2021b), an additional heating process in the IHS (Chalov et al. 2003; Zirnstein et al. 2018a), a separate ENA source from outside the heliopause (Izmodenov et al. 2009; Opher et al. 2013; Zirnstein et al. 2014), or some combination of these. We address this issue by utilizing a dynamic model of PUI transport through the heliosphere to simulate the origin and evolution of IBEX ENA observations.

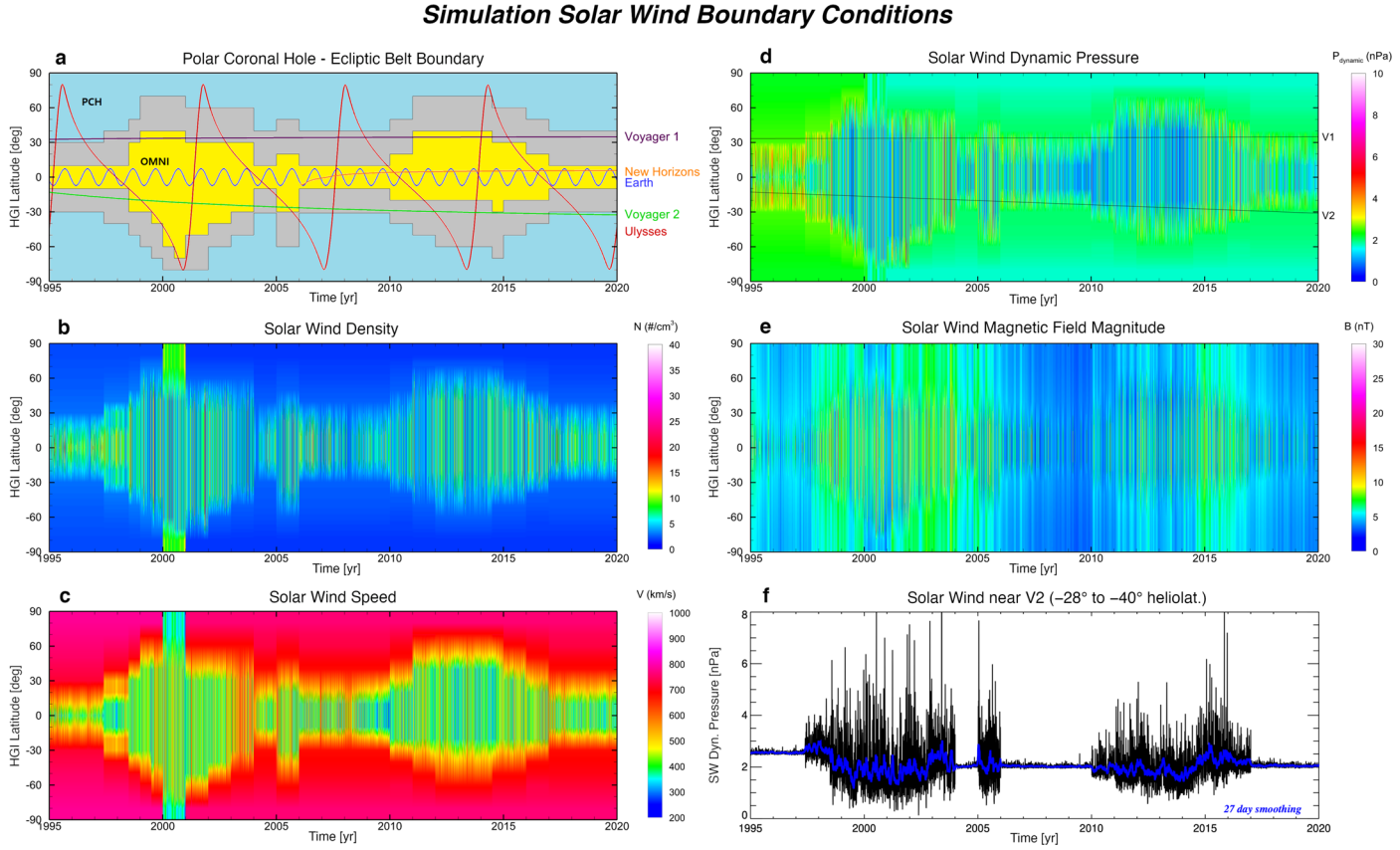

Figure 1. Time series of the latitude distribution of the SW boundary conditions at 1 au. (a) Contours identifying the streamer belt region where OMNI data are applied (yellow); the PCH region constrained by Ulysses observations up to 2009, where SW conditions from SC23 are repeated after 2009 (blue); and the linearly interpolated filler region between OMNI and PCH data (gray). (b)–(e) SW density, speed, dynamic pressure, and magnetic field magnitude. (f) SW dynamic pressure conditions averaged over a range near Voyager 2's latitude. A 27 day running boxcar smoothing of the pressure is shown in blue.

2. Model Description

We utilize a three-dimensional (3D), time-dependent magnetohydrodynamic (MHD) simulation of the heliosphere to simulate the transport of the bulk SW plasma across the HTS and through the IHS. The dynamic flow streamlines of the MHD plasma are then used to model the transport of PUIs and ENAs for our analysis of IBEX data. Based on the Multi-scale Fluid-Kinetic Simulation Suite (MS-FLUKSS; Pogorelov et al. 2014), the heliosphere model utilizes adaptive mesh refinement to efficiently simulate the propagation of SW, including transient structures, through the outer heliosphere on a sufficiently high-resolution grid. The SW observations from the OMNI database and Ulysses data are used to drive and constrain the time-varying inner boundary conditions at 1 au, with both longitudinal and latitudinal variations (Kim et al. 2016, 2017; see Figure 1). The outer boundary conditions are derived from IBEX-Lo observations of the interstellar neutral gas (McComas et al. 2015) and IBEX-Hi observations of the ribbon (Zirnstein et al. 2016). A description of the MHD heliosphere simulation is given in Appendix A.

We solve for the advection, compression, and heating of PUIs at the HTS and in the IHS along streamlines in the MHD simulation as a function of time. We use an empirical PUI heating prescription to define how PUIs are heated at the shock and in the IHS. First, we define an initial proton distribution function downstream of the HTS, $f_p(\boldsymbol{r}_0, v_0, t_0)$, as a kappa function, as shown in Figure 2(a). In the IBEX-Hi energy range, the test particle simulation results from Zirnstein et al. (2021b) are well fit by a kappa distribution with kappa index $\kappa = 2.4$. While κ may vary over time, we assume it is invariant and instead vary the distribution temperature. The proton temperature downstream of the HTS is derived from the upstream temperature using a polytropic heating relation,

$$T_0(\boldsymbol{r}_0, t_0) = T_u(\boldsymbol{r}_0, t_0)[R(\boldsymbol{r}_0, t_0)]^{\gamma_{\rm HTS}-1}, \quad (1)$$

where $R(\boldsymbol{r}_0, t_0)$ is the local HTS compression ratio from the MHD simulation, $\gamma_{\rm HTS}$ is the prescribed polytropic heating index at the HTS, and $T_u(\boldsymbol{r}_0, t_0)$ is the upstream effective proton temperature. Next, according to SWAP observations, interstellar H^+ PUIs can be described by a generalized filled-shell distribution (McComas et al. 2021). The PUIs have undergone heating in the expanding SW and can be defined using a nonadiabatic "cooling index" $\alpha > 3/2$, which extrapolates to $\alpha \cong 2.9$ at the HTS. Using the generalized filled-shell distribution from McComas et al. (2021) and the local SW speed upstream of the HTS from the MHD simulation, $u_{u,\rm SW}(\boldsymbol{r}_0, t_0)$, the upstream H^+ PUI temperature can be calculated analytically as (Zirnstein et al. 2022)

$$T_{{\rm PUI},u}(\boldsymbol{r}_0, t_0) = \frac{m_{\rm H}}{3k_B} V_{\rm inj}^2(\boldsymbol{r}_0, t_0) E_{2+2/\alpha}(\Lambda) \times [\exp(-\Lambda) - \Lambda E_1(\Lambda)]^{-1},$$
$$\Lambda = \frac{\lambda_{\rm H}}{r_0} \frac{\theta}{\sin\theta}, \quad (2)$$

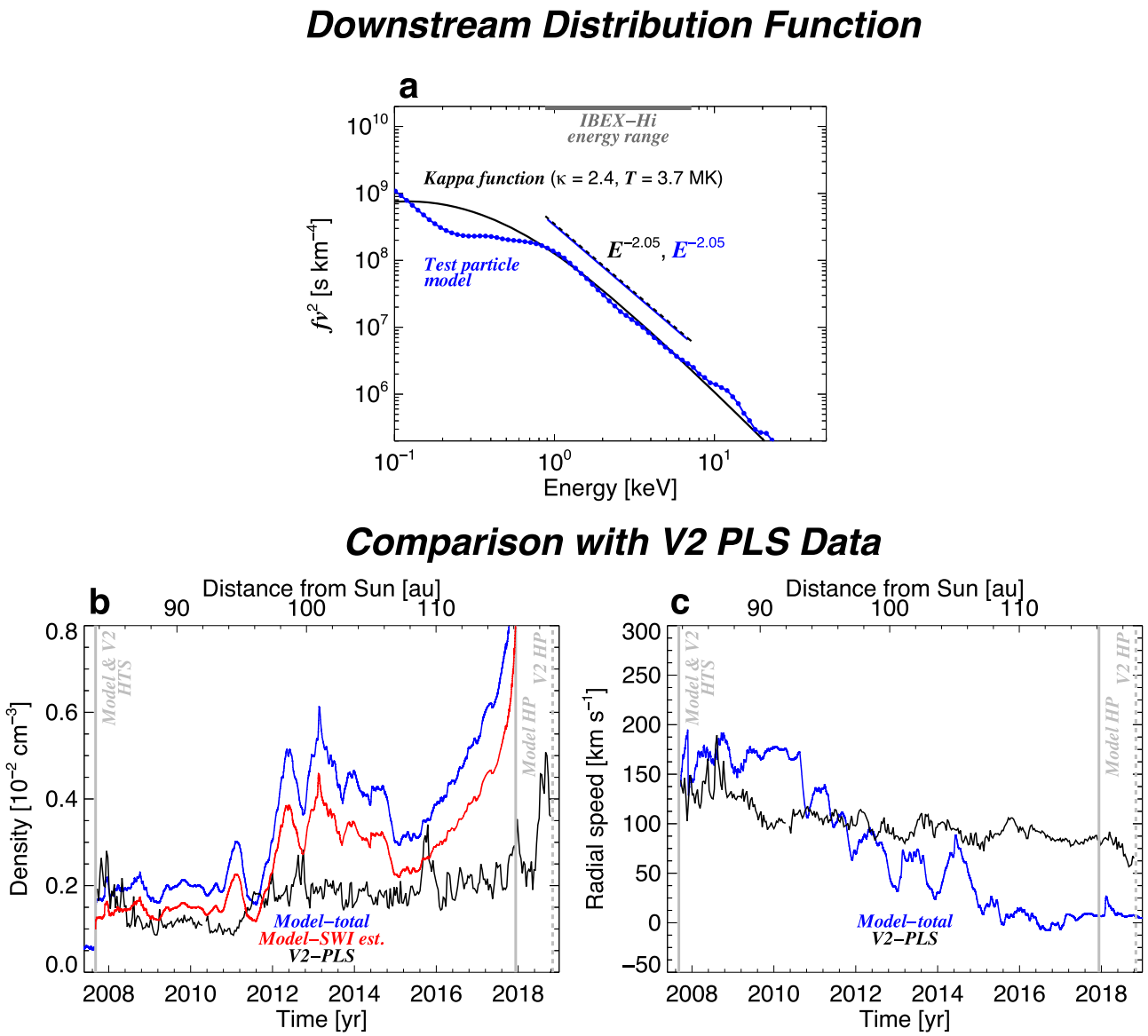

Figure 2. (a) Test particle simulation results of SWIs (<0.2 keV) + PUIs (>0.2 keV) accelerated at the HTS in the direction of Voyager 2 (Zirnstein et al. 2021b), shown in the downstream plasma frame. A kappa function with index $\kappa = 2.4$ and temperature 3.7×10^6 K is shown to fit well to the test particle results. Slopes of the two distributions in the IBEX-Hi energy range are also shown. (b) and (c) Plasma density and speed from the MHD simulation compared to Voyager 2 PLS observations in the IHS. Because V2 PLS cannot observe PUIs, we scale the MHD density by 0.75 in panel (b) to approximate a better comparison ("Model-SWI est."). The simulated and observed HTS and heliopause boundary distances are also shown.

where $V_{\rm inj}(\boldsymbol{r}_0, t_0) \cong u_{u,\rm SW}(\boldsymbol{r}_0, t_0)$, $E_y(x)$ is the exponential integral, $\lambda_{\rm H} = 4$ au is the interstellar H ionization cavity size (Swaczyna et al. 2020), and θ is the angle between $\boldsymbol{r}_0$ and the LISM H upwind vector (Lallement et al. 2010). We keep the SW temperature constant at $T_{{\rm SWI},u}(\boldsymbol{r}_0, t_0) = 10^4$ K based on Voyager 2 measurements (Richardson et al. 2008). The total effective proton temperature upstream of the HTS is calculated as

$$T_u(\boldsymbol{r}_0, t_0) = (1 - \Gamma) \times T_{{\rm SWI},u}(\boldsymbol{r}_0, t_0) + \Gamma \times T_{{\rm PUI},u}(\boldsymbol{r}_0, t_0), \quad (3)$$

where $\Gamma = n_{\rm PUI}/(n_{\rm SWI} + n_{\rm PUI})$ is the local H^+ PUI density ratio. The MHD simulation does not keep track of the separate densities of SWIs versus PUIs; therefore, we estimate the time-dependent PUI density ratio as

$$\begin{aligned}\Gamma(\boldsymbol{r}_0, t_0) &= \frac{r_{\rm HTS}}{n_{1\,\rm au} u_{1\,\rm au}} \langle n_{\rm H} \rangle \times [\nu_{{\rm ph},1\,\rm au} + n_{1\,\rm au} u_{1\,\rm au} \sigma_{\rm ex}(v_{\rm rel})], \\ u_{1\,\rm au} &= u_{u,\rm SW} \Big/ \left(1 - \left(1 - \frac{1}{2}\frac{\gamma - 1}{2\gamma - 1}\right)\frac{r_{\rm HTS}}{\lambda}\right), \\ &\cong u_{u,\rm SW} \Big/ \left(1 - \left(1 - \frac{1}{2}\frac{\gamma - 1}{2\gamma - 1}\right)\Gamma^*\right), \\ n_{1\,\rm au} &= n_{u,\rm SW} \frac{u_{u,\rm SW} r_{\rm HTS}^2}{u_{1\,\rm au} r_{1\,\rm au}^2}. \end{aligned} \quad (4)$$

The PUI density ratio equation (first in Equation (4)) and the slowing of the SW speed due to mass loading by PUIs (second

in Equation (4)) are first-order solutions to the single fluid transport equations (Lee et al. 2009). The third equation is derived from mass flux conservation assuming that PUI production by photoionization is small. The relative speed of interaction is $v_{\rm rel} \cong u_{u,\rm SW}$, λ is the mean free path for PUI mass loading, and $\gamma = 5/3$. The time-dependent photoionization rate for neutral H, $\nu_{\rm ph,1\ au}$, is extracted from TIMED/SEE data and the F10.7 index (Sokół et al. 2020). We use a constant value of the interstellar H density $\langle n_{\rm H} \rangle = 0.1\,{\rm cm}^{-3}$ representing the average value between the Sun and HTS. The PUI density ratio can be written in terms of the mean free path as $\Gamma = r_{\rm HTS}/\lambda$. Because the MHD simulation assumed an older and underestimated value for the interstellar H density (yielding $\sim 0.09\,{\rm cm}^{-3}$ at the HTS instead of $0.13\,{\rm cm}^{-3}$; Swaczyna et al. 2020), we substitute $\Gamma^* = \Gamma \times (n_{\rm H,HTS}/0.13\ {\rm cm}^{-3})$ in Equation (4), where $n_{\rm H,HTS}$ is the simulation H density at the HTS, and $0.13\,{\rm cm}^{-3}$ is the observed value extrapolated from SWAP.

We note that the PUI density ratio must first be known to calculate the slowing of the SW speed. Therefore, we undergo an iterative procedure of solving Equation (4) by first assuming $\Gamma^* = 0.25 \times (n_{\rm H,HTS}/0.13\ {\rm cm}^{-3})$, solve for the SW speed and density at 1 au, and then repeat with the new estimate for $\Gamma(\boldsymbol{r}_0, t_0)$ in Equation (4) until convergence is reached. Convergence is defined when two successive iterations of $\Gamma(\boldsymbol{r}_0, t_0)$ yield values within 0.01. The results of this method yield values close to 20%–30% at the HTS over the solar cycle, which appear consistent with extrapolations from SWAP observations (McComas et al. 2021). We note that our method does not include the small acceleration of the bulk SW due to pressure gradients from interstellar PUIs (Zank et al. 2018).

The proton distribution in the IHS is calculated according to

$$f_p(\boldsymbol{r}, t, n, T) = f_p(\boldsymbol{r}_0, t_0, n, T) \times \exp\left[-\int_0^l n_{\rm H} \sigma_{\rm ex}(v_{\rm rel}) \frac{v_{\rm rel}(v', l', t')}{u_{\rm MHD}(l', t')} dl' \right], \quad (5)$$

where $n = n_{\rm MHD}$ and $u_{\rm MHD}$ are the MHD plasma density and speed, $n_{\rm H} = 0.13\,{\rm cm}^{-3}$ is the average interstellar neutral H density in the IHS, $v_{\rm rel}$ is the relative speed of interaction during charge exchange (Zirnstein et al. 2018a), and $\sigma_{\rm ex}$ is the energy-dependent charge exchange cross section. The PUI distribution at position vector $\boldsymbol{r}$ and time t in the IHS is solved as a function of density compression (replacing n_0 with n), losses due to charge exchange during advection with the bulk MHD plasma velocity, and heating/cooling by compression/expansion. The latter's effect on the distribution temperature T and particle speed v' in the exponential term is calculated using the polytropic relation

$$T(\boldsymbol{r}, t) = T_0(\boldsymbol{r}_0, t_0) \left[\frac{n_{\rm MHD}(\boldsymbol{r}, t)}{n_{\rm MHD}(\boldsymbol{r}_0, t_0)} \right]^{\gamma_{\rm IHS}-1},$$
$$v'(l', t') = v(l, t) \left[\frac{n_{\rm MHD}(l', t')}{n_{\rm MHD}(l, t)} \right]^{(\gamma_{\rm IHS}-1)/2}, \quad (6)$$

where we test values for the polytropic index $\gamma_{\rm IHS}$ between 5/3 and 2 based on studies of PUI heating at shocks in the IHS (Mostafavi et al. 2019). We find that IHS heating is not as important as HTS heating and set $\gamma_{\rm IHS} = 5/3$ as a constant over time for our main results. After solving Equation (5), we integrate the differential ENA flux at 1 au and compare to IBEX-Hi ENA observations collected from 2009 to 2020 (McComas et al. 2020). Descriptions of the ENA flux equation and IBEX data are given in Appendix B.

Comparisons between simulated plasma density and speed in the IHS with Voyager 2 measurements are shown in Figures 2(b) and (c). Because the MHD density includes both SW and PUIs, we also show modeled densities scaled by 0.75 to estimate the SW-only density in the IHS. There is a significant discrepancy between densities in ~2012–2015 and closer to the heliopause. However, because of the continued loss of SW protons by charge exchange in the IHS, plasma science experiment (PLS) measurements may underestimate the plasma density closer to the heliopause, where more injected PUIs are created (Zirnstein et al. 2014). Therefore, comparisons are not straightforward. The plasma radial speeds are also significantly different between the model and data, where the model overestimates the speed before 2011 and underestimates after 2012. Interestingly, the modeled speeds compare better to speed estimations from the low-energy charged particles and cosmic ray subsystem (Cummings et al. 2021; Richardson et al. 2021). The largest discrepancy in speeds occurs after 2016 but likely does not significantly affect our results because the majority of ENAs created after 2015 are from the inner half of the IHS (Figure 3).

3. Results and Discussion

Examples of the simulated PUI density in the IHS along the Voyager 2 direction are shown in Figure 3. The MHD plasma density and speed are shown in black, and the simulated PUI partial density between 2 and 6 keV (corresponding to IBEX-Hi electrostatic analyzer (ESA) 5–6 energy ranges) is shown in blue.

The PUI distribution in the IHS evolves with the solar cycle due to nonadiabatic heating at the HTS; near-adiabatic heating in the IHS; effects from charge exchange, which are significantly more prominent closer to the heliopause; and dynamic SW events. Before ~2010, Voyager 2's heliolatitude was close to the southern polar coronal hole (PCH) boundary, where a predominantly fast and steady SW was propagating to the outer heliosphere. The PUIs formed a filled shell with a relatively large speed cutoff equal to the fast SW speed. These PUIs become a relatively hot distribution downstream of the HTS due to the large cutoff speed, yielding large densities at energies above 2 keV (Figure 3(a)). The PUI distribution in the IHS exhibits only small fluctuations in the fast but steady SW. After ~2010 at the Sun, the SW becomes more variable from increased stream interactions at Voyager 2's heliolatitude, leading to lower density but more variable PUI distributions in the IHS after 2011 (Figures 3(b)–(e)). Then, in late 2014, the SW experienced a large increase in dynamic pressure that propagated to the outer heliosphere and produced a clear and expanding ENA emission enhancement starting a couple years later (McComas et al. 2018b, 2020). This increase in pressure becomes visible in the simulated PUI distribution beginning in early 2015 and propagates through the IHS over the following years.

Smaller, transient increases in PUI density also propagate through the IHS at various times throughout the solar cycle. For example, the peak in PUI density near ~95 au in 2013.0 is

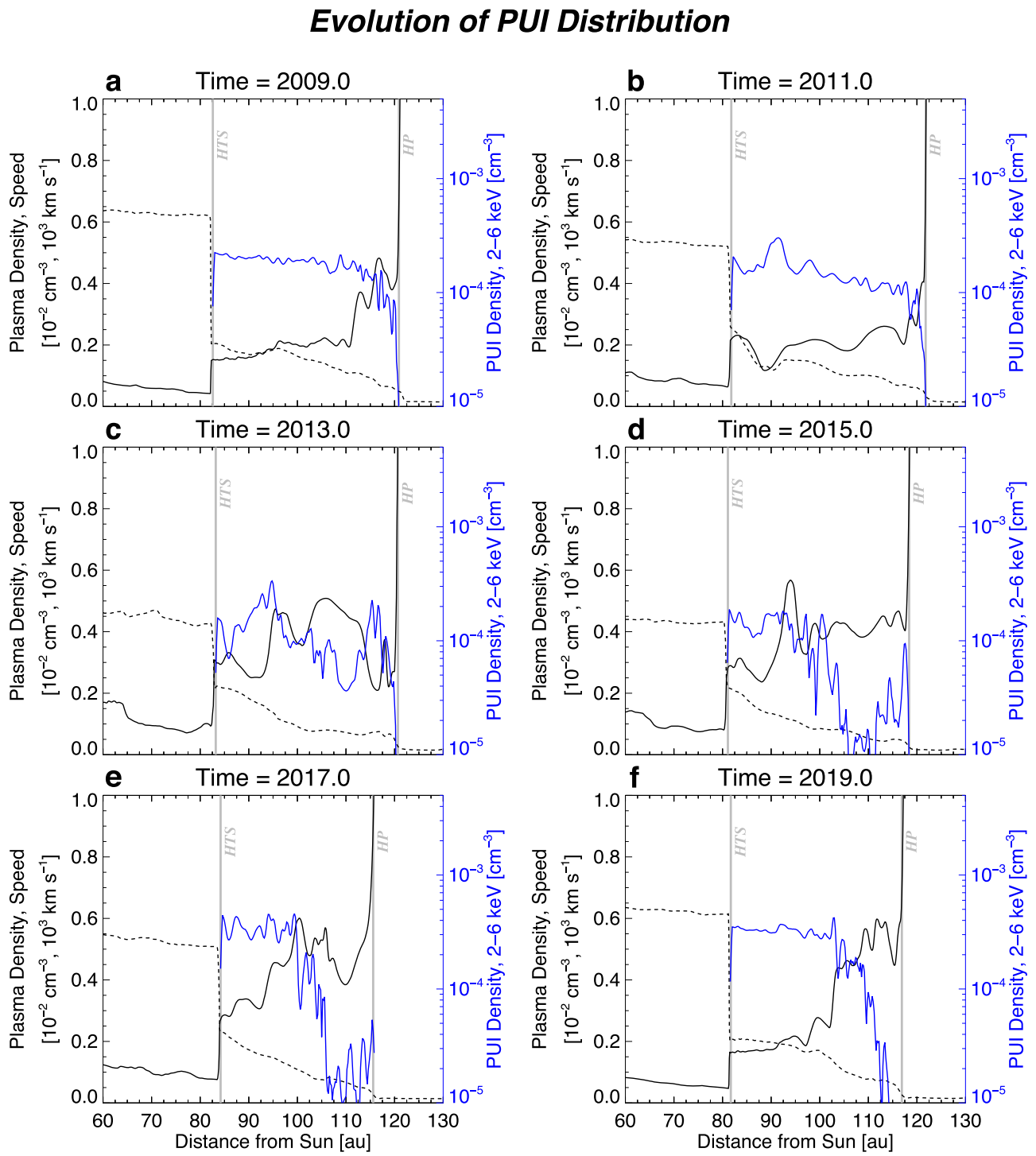

Figure 3. The MHD plasma density (solid black), speed (dashed black), and partial PUI density from 2 to 6 keV (solid blue) at various times in the simulation. The PUI energy range approximately coincides with ENAs observed by IBEX at ESA 5–6.

caused by a merged interaction region formed by solar transients that reached the HTS in ∼2012.9. Interestingly, this SW structure also produced the shock jump in magnetic field observed by Voyager 1 in the VLISM in mid-2014 ("sh2" in Burlaga et al. 2022, and reproduced by Kim et al. 2017). Another example is the peak in PUI density near ∼90 au in 2011.0. This is created by the sudden change in SW boundary conditions at 1 au in ∼2010.0 (see Figure 1(f)), where the PUI density ratio in the IHS briefly increased due to a large fluctuation in the HTS distance.

Figure 4 shows simulated ENA fluxes at 1 au for IBEX-Hi ESA passbands 2–6. We first note that we made two important assumptions in our model. First, the PUI distribution is heated at the HTS using a polytropic relation as described in Section 2. We performed a sensitivity analysis using χ^2 minimization to determine the polytropic indices that yield the best model fit to the data (see Appendix C). We chose two time periods over solar cycle 24 where the SW exhibited significantly different behavior ($T < 2014.75$ and >2014.75) and set the heating index within these periods to different values. In ∼2014.75, a

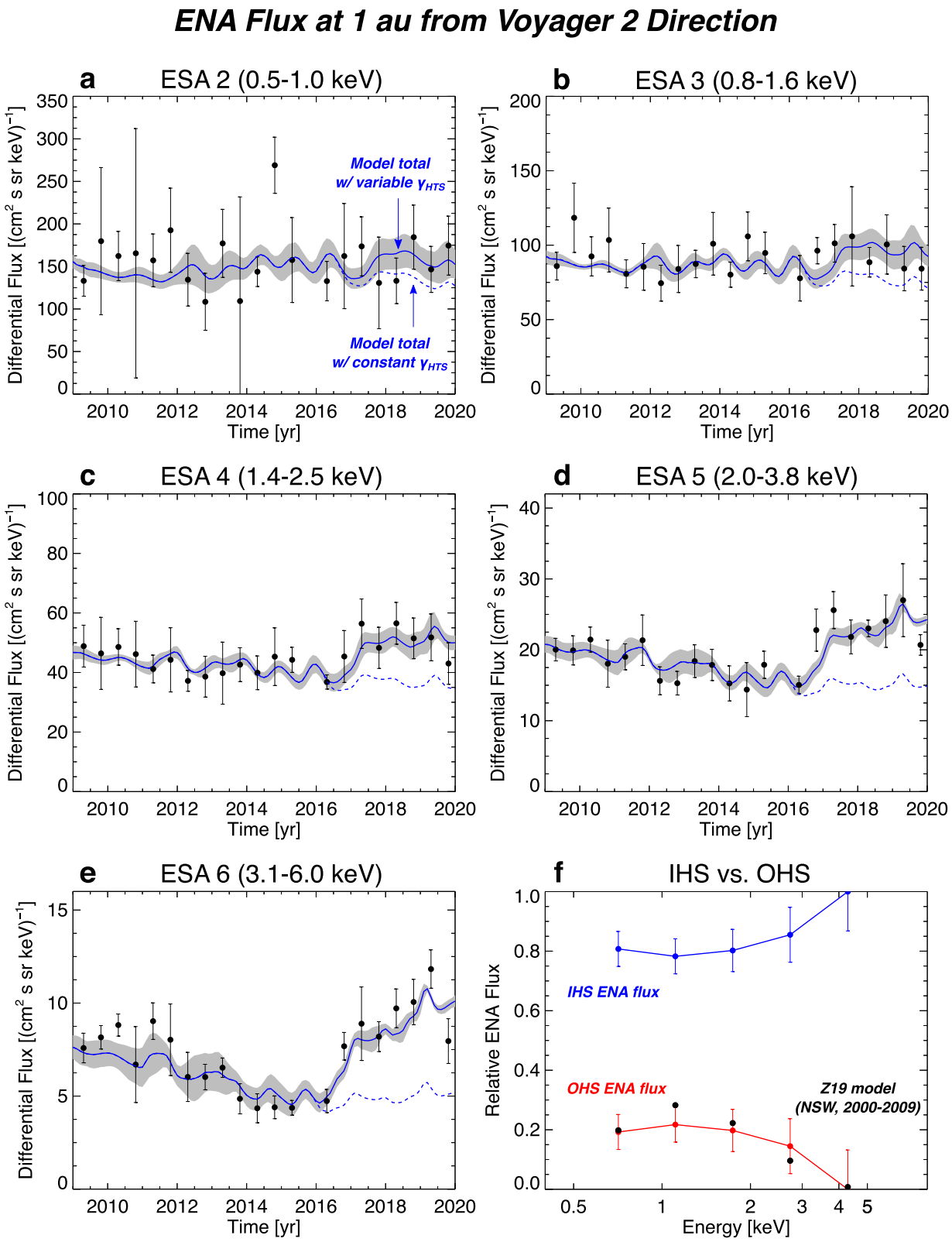

Figure 4. (a)–(e) IBEX-Hi observations of ENA fluxes from directions near Voyager 2 (black dots with uncertainties) and simulated ENA fluxes (solid blue curves with gray uncertainty shaded regions) from the IHS plus a constant background added to match IBEX data averaged over time. The data uncertainties represent the weighted standard deviation of fluxes in the nearest 9 pixels. The gray shaded regions around the simulated fluxes represent the standard deviation of the fluxes over the same pixels as the data. This simulation assumed $\gamma_{HTS} = 2.3$ and 2.7 for $T < 2014.75$ and >2014.75, where T is the SW time at 1 au. Examples of simulated fluxes assuming $\gamma_{HTS} = 2.3$ over all times are shown as dashed blue curves. (f) Relative contribution of ENA fluxes from the IHS vs. OHS, assuming that the OHS ENA flux is constant over time. Uncertainties of the model fit to the data are also shown. The OHS ENA model results from Z19 are also shown as black dots. The Z19 model is the case where the pitch angle scattering rate outside the retention region is much larger than the charge exchange rate.

large increase in SW dynamic pressure was released from the Sun and lasted for several years. Test particle and particle-in-cell simulations suggest that the polytropic heating index γ_{HTS} of the SWI + PUI mixture is between ~2.0 and 2.5 (Wu et al. 2009; Yang et al. 2015; Kumar et al. 2018; Zirnstein et al. 2021b) and likely depends on the PUI density ratio, plasma Mach number, and magnetic turbulence power. We find from our analysis that the first period ($T < 2014.75$) yields $\gamma_{HTS} = 2.31 \pm 0.09$, and the second period ($T > 2014.75$) required a higher index of $\gamma_{HTS} = 2.70 \pm 0.07$. We note that choosing two time periods with constant heating indices is a simplification, but it should reasonably demonstrate the average heating indices. Figure 4 also shows results where we assumed $\gamma_{HTS} = 2.3$ over the entire time period of the simulation (dashed blue curves), assuming the same separate ENA source values as the variable case, which significantly underestimate IBEX observations after 2016.

The second assumption we made in our model is that there may be a separate ENA source, not from the IHS. We assume the separate ENA source is approximately constant, or at least not significantly changing, over the considered observation time. We therefore add a constant flux parameter with different values for each ESA in the χ^2 minimization process. The possible origin of this source is discussed in more detail below, which we propose comes from the outer heliosheath (OHS).

With these two key assumptions, our model of ENA fluxes can reproduce IBEX-Hi observations. At ESA 2, the ENA fluxes at 1 au appear to be relatively constant over the course of the solar cycle but exhibit nearly random variability at small timescales (~1 yr). The variability is driven by changes in the PUI pressure in the IHS and the thickness of the ENA source along the detector line of sight (LOS). The ENA fluxes at ESA 3 are similar in behavior. At ESA 4, the evolution of the ENA fluxes begins to show a systematic decrease from 2009 to 2016 and a significant increase after 2016. This behavior becomes more pronounced at ESA 5 and 6. As we described earlier, the rise in ENA flux after 2016 is in response to a large increase in SW dynamic pressure at 1 au in late 2014 (McComas et al. 2018b). To reproduce the IBEX observations, we required a significant increase in the HTS heating index from ~2.3 to 2.7. This suggests that a physical change in the heating of PUIs at the HTS might occur in concert with the SW dynamic pressure. We tested using the Rankine–Hugoniot jump conditions with input from the MHD solution (upstream plasma pressure, Mach number, etc.) and found that the jump conditions underpredicted the heating index required to reproduce the IBEX data, especially after 2016. This is likely related to the fact that Rankine–Hugoniot jump conditions do not formally apply to nonthermal distributions like PUIs. Therefore, it is possible that a separate mechanism is responsible for the change in heating index, such as enhanced turbulence at the HTS (Zirnstein et al. 2021b). The sensitivity of our results on the SW boundary conditions was also tested using the simulation from Kim et al. (2017), where we find best-fit HTS heating indices of ~2.3 and 2.5. This suggests that the HTS heating index may be between ~2.5 and 2.7 for the second time period in cycle 24.

The separate ENA source contribution to the model, which we interpret as an OHS ENA source, is quantified in Figure 4(f). On average, over ESA 2–6, the OHS ENA contribution is approximately $\lesssim$20%, while $\gtrsim$80% of the ENA flux observed by IBEX-Hi originates from the IHS. Results from the spatial retention model of the ribbon presented by Zirnstein et al. (2019, hereafter Z19), originally developed by Schwadron & McComas (2013), are shown as black dots in Figure 4(f). This particular model is the case where the pitch angle scattering rate of PUIs outside the retention region is much higher than the charge exchange rate (see Figures 6–8 in Z19). The secondary ENA model predicts similar fluxes as the current analysis, supporting the idea that secondary ENAs can explain the missing ENA fluxes observed by IBEX. Our analysis, however, comes with significant uncertainties, especially at higher ENA energies. This is because of the strong sensitivity of higher-energy particles to the polytropic heating index. If the contribution of OHS ENA fluxes is as large as ~10%–20% at ~2–6 keV, we propose that primary ENAs from (1) the hot heliosheath and (2) PUIs in the supersonic SW region may be important to include in the secondary ENA source model. Primary ENAs that escape the heliosphere form the parent protons of the secondary ENA population. The Z19 model only includes primary ENAs from the neutralized supersonic SW, which dominates the ~1 keV distribution at the latitude of Voyager 2. However, as shown by Schwadron & McComas (2019), primary ENAs from interstellar PUIs in the supersonic SW, as well as the hot heliosheath, can dominate the neutral H distribution propagating to the OHS at energies >2 keV.

In contrast to the OHS ENAs, whose source extends over large distances from the heliopause (Z19), ENA emissions from the IHS respond more strongly over time to changes in the IHS plasma properties. In particular, the evolution of the (1) thickness of the IHS and (2) mean PUI distribution through the IHS govern the evolution of the ENA spectrum observed near 1 au. This behavior is demonstrated in Figure 5, where we show the model partial proton pressure (at energies corresponding to ESA 2 and 6), as well as the pressure times ENA source thickness. The scaled model ENA fluxes at ESA 2 and 6 are also shown for comparison. First, the ESA 2 ENA fluxes show significant temporal fluctuations between 2012 and 2016 in response to solar transients propagating at the latitude of Voyager 2 through the IHS. The ENA emissions show less variability before 2012, when the southern PCH was closer to the latitude of Voyager 2 and SW variability was small. The ENA emissions observed at ESA 6 show less short-term variability in 2012–2016 but more significant changes over longer timescales. Both are correlated with the IHS-averaged proton pressure before 2016.

However, after 2016, partial proton pressures averaged through the IHS and ENA emissions at 1 au become less correlated because the large increase in SW dynamic pressure in late 2014 caused a dramatic change in the IHS thickness, pushing the HTS outward with no immediate change in the heliopause. This caused a decrease in ENA source thickness and dampened the rapid rise in ENA flux at 1 au. Eventually, the IHS thickness increased as the heliopause moved outward and the IHS pressure rebalanced, further increasing the ENA emissions over a period of $\gtrsim$3 yr after the initial rise.

4. Conclusions

Using a dynamic, data-driven 3D simulation of the global heliosphere, we have reproduced the evolution of ENA fluxes observed by IBEX-Hi between ~0.5 and 6 keV by assuming a specific variation in the effective heating of PUIs at the HTS over the solar cycle; this variation required polytropic heating indices that varied from ~2.3 to possibly as high as 2.7 to

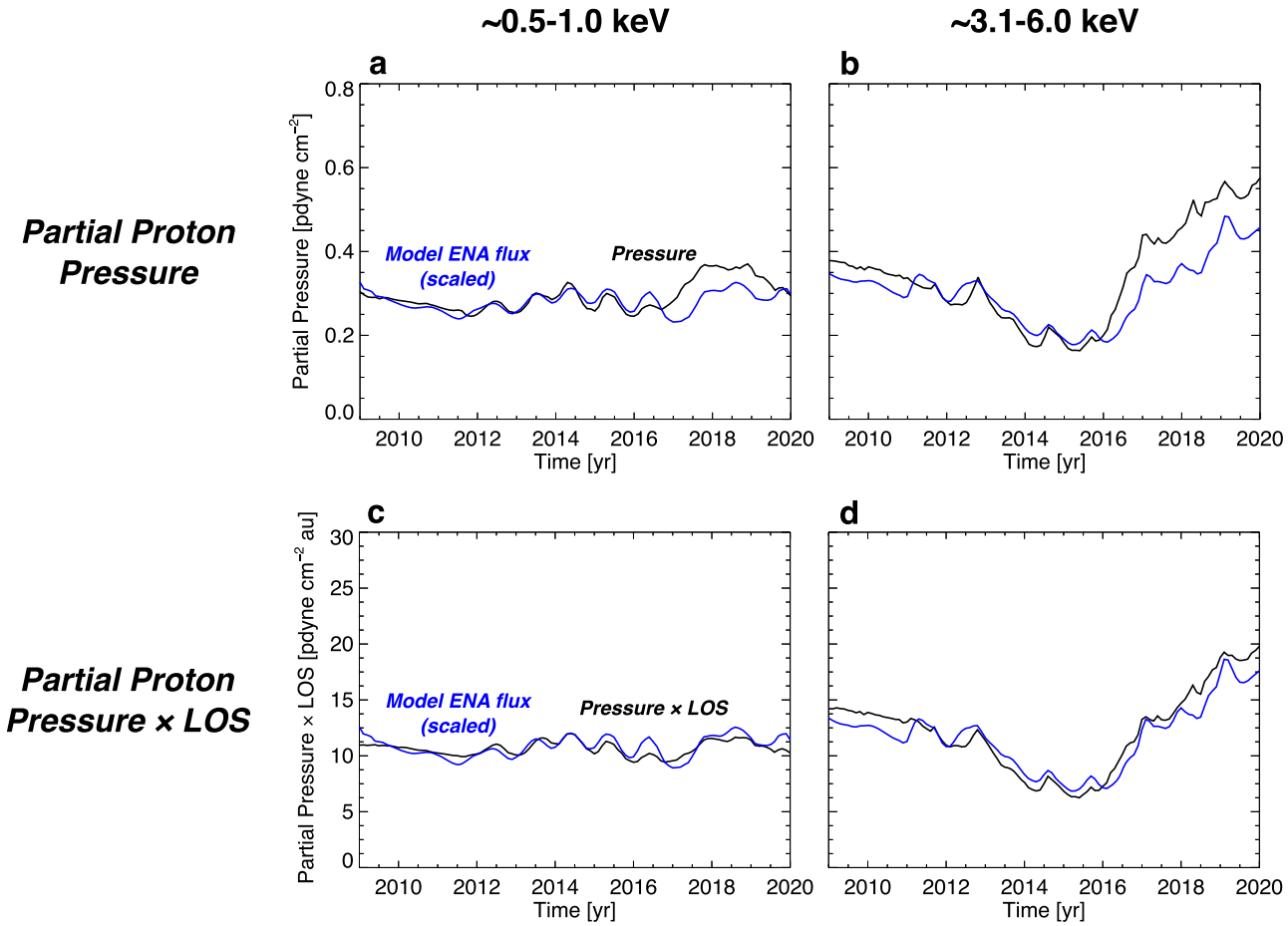

Figure 5. (a) and (b) LOS-integrated partial proton pressure (black) and simulated ENA flux (blue) from a single pixel for 0.5–1 (ESA 2) and 3.1–6 (ESA 6) keV. Partial pressures are integrated through the ENA source region in the IHS at the local ENA creation times at energies in the center of the energy range (0.7 and 2 keV, respectively). (c) and (d) Similar to panels (a) and (b), except the partial pressure is integrated over the respective ENA source thickness along the LOS. The model ENA fluxes are scaled such that the ENA flux averaged over 2009–2016 equals that of the partial pressure (or partial pressure times LOS).

match the IBEX data. The assumed heating index appears to be correlated with the SW dynamic pressure and large-scale behavior of the PCH. The ENAs between 0.5 and ∼1.5 keV do not show significant long-term evolution over time but mostly short-term fluctuations on a scale of ∼1 yr. Above ∼1.5 keV, ENA fluxes show long-term variations with the solar cycle. This disparity between the evolution of low- (<1.5 keV) and high- (>1.5 keV) energy ENAs suggests that higher-energy PUIs respond more strongly to variations in the heating and acceleration processes at the HTS and are more correlated with solar cycle changes in the polytropic heating index at the HTS.

To match IBEX observations, we required a separate source of ENA fluxes, which we assumed was constant over time for simplicity. This source is approximately $\lesssim$20% of the total ENA intensity in the direction of Voyager 2 between 0.5 and 6 keV. Secondary ENA models based on the spatial retention of PUIs outside the heliopause, such as that presented by Z19, appear to agree with our analysis. Secondary ENA models also suggest the importance of including neutralized interstellar PUIs and heliosheath protons in secondary ENA models to analyze ENA observations at higher energies. Another improvement to our analysis would be to allow for gradual changes in the OHS component, which are shown to exist in the evolution of the ribbon (Schwadron et al. 2018) and therefore are likely to occur for the OHS-GDF component.

The results shown in this study stress the importance of modeling the time dependence of PUIs in the presence of solar transients and the evolving solar cycle to explain IBEX observations. In a future study, we plan to identify specific transient events in Voyager in situ observations that can be connected to IBEX ENA observations. It has already been suggested that a pressure enhancement observed by Voyager 2 in the IHS in late 2015 is related to the large increase in SW dynamic pressure in late 2014 (Richardson et al. 2017), which represents the biggest event in IBEX ENA observations (McComas et al. 2018b). Other transient events observed by Voyager 1 and 2 while inside the IHS, or even outside the heliopause, may be connected to IBEX observations with sophisticated dynamic modeling of the heliosphere. Connections between solar events and ENA measurements can be improved even more with future measurements by the Interstellar Mapping and Acceleration Probe (McComas et al. 2018a).

E.J.Z., T.K.K., M.A.D., and J.S.R. acknowledge support from NASA grant 80NSSC20K0783. E.J.Z., M.A.D., and P.S. acknowledge support from NASA grant 80NSSC21K0582. E.J.Z. also acknowledges partial support from NASA grants 80NSSC17K0597 and 80NSSC21K1686, and T.K.K. acknowledges partial support from NASA grant 80NSSC20K1453. This work was also partially supported by the NASA IBEX

Mission (80NSSC20K0719), which is part of the Explorers Program. Global MHD simulations were performed with supercomputer allocations provided by NASA High-End Computing Program award SMD-20–92772410 and NSF XSEDE project MCA07S033. We acknowledge the NASA/GSFC Space Physics Data Facility's OMNIWeb for the solar wind and magnetic field data used in this study. E.J.Z. thanks Rahul Kumar and George Livadiotis for helpful discussions and Justyna Sokół for providing the H photoionization rate data.

Appendix A
3D Dynamic Simulation of the Heliosphere

The MHD heliosphere simulation utilized in this study is based on the MS-FLUKSS (Pogorelov et al. 2014), which was adapted by Kim et al. (2016, 2017) to simulate the propagation of SW structures (e.g., coronal mass ejections, corotating interaction regions, and globally merged interaction regions) through the outer heliosphere. The heliosphere simulation solves the ideal MHD equations for the plasma and separate Euler equations for four neutral H fluids originating from the supersonic SW, IHS, OHS, and LISM. The plasma and neutral fluids are solved iteratively and coupled by charge exchange source terms in the momentum and energy equations (Pauls et al. 1995; Pogorelov et al. 2006).

The simulation spatial grid is similar to that used in previous studies by Kim et al. (2016, 2017). The simulation domain is solved on a spherical grid with adaptive spatial resolution to resolve SW structures near the IHS. We focus our study on the LOS near Voyager 2's trajectory, with a radial grid resolution between $\Delta r \cong 0.05$ and 0.1 au in the IHS and an angular resolution of $\sim 0.^{\circ}7$, which is reduced to $\sim 2^{\circ}$ for the PUI/ENA flux calculations.

Time-dependent SW boundary conditions at 1 au are extracted from two sources: (1) the OMNI SW database of daily averaged observations near the ecliptic plane and (2) Ulysses observations at high latitudes (McComas et al. 2008). The inner boundary conditions are divided into three latitudinal domains, as shown in Figure 1(a) (see also Kim et al. 2017). OMNI-derived SW properties (plasma density, speed, temperature, magnetic field) are applied at low latitudes in the yellow region surrounding the ecliptic plane. The blue region is constrained to best match Ulysses observation high latitudes using methodology from Pogorelov et al. (2013; up until 2009). The midlatitude gray region linearly interpolates between the OMNI-driven yellow and Ulysses-constrained blue regions (Kim et al. 2016). After 2009, it is assumed that the SW properties fit to Ulysses observations at high latitudes in the preceding solar cycle 23 recur, and the gray region is interpolated the same way as before. Examples of the simulation boundary conditions are shown in Figure 1.

The latitudinal extent of the fast SW from the PCHs (blue in Figure 1(a)) is not known beyond 2009 without any in situ spacecraft instrument but has been estimated from extreme-ultraviolet observations from the Solar Dynamics Observatory (Karna et al. 2014) and interplanetary scintillation observations (Sokół et al. 2020; Tokumaru et al. 2021). Therefore, we test different variations of the latitudinal extent of the PCH in the southern hemisphere (the northern hemisphere does not affect our analysis) and study their effect on our PUI-ENA model. We did not find any significant effects of different latitude boundaries of the PCH on our ENA results, primarily because the dominant source of change after 2009 is the SW pressure increase in 2014 and our evolving polytropic heating index. Specifically, we tested our analysis using the SW boundary conditions from Kim et al. (2017), whose SW conditions are symmetric in the northern and southern hemispheres. We note that while SW conditions upstream of the HTS from Kim et al. (2017) better match Voyager 2 observations (see, e.g., Figure 3 in Kim et al. 2016 using similar SW conditions), the predicted HTS crossing is earlier by a couple years. The SW conditions were altered in the current study to better match the HTS crossing by Voyager 2 by extending the southern PCH to lower latitudes in 2004–2005 and 2006–2007 (compare Figure 1(a) in this study to Figure 1 in Kim et al. 2017). Our ENA flux χ^2 analysis yields statistically consistent HTS heating indices before 2014.75 ($\gamma_{\rm HTS} \sim 2.3$ for both heliosphere simulations) and slightly smaller heating indices after 2014.75 for Kim et al. (2017) SW conditions ($\gamma_{\rm HTS} \sim 2.5$ instead of 2.7). The separate ENA source levels are also statistically consistent using results from both heliosphere simulations.

The outer boundary conditions of the simulation at 1000 au from the Sun are assumed to be time-independent. The LISM plasma and neutral H flow direction ($255.^{\circ}7$, $5.^{\circ}1$), speed (25.4 km s^{-1}), and temperature (7500 K) are derived from IBEX-Lo observations (McComas et al. 2015) and the effective plasma and neutral H densities (0.09 and 0.154 cm^{-3}, respectively) from Zirnstein et al. (2016). We note, however, that this neutral H density value underestimates the new, higher density derived by Swaczyna et al. (2020) by ~30%–40%. Therefore, when simulating ENA fluxes from our PUI model, we set the neutral H density in the IHS to 0.13 cm^{-3}. The interstellar magnetic field magnitude (3 μG) and direction ($226.^{\circ}99$, $34.^{\circ}82$) far from the heliosphere are derived from the ribbon fitting analysis by Zirnstein et al. (2016).

Appendix B
ENA Flux Model and Data

The differential ENA flux at ENA speed $v_{\rm ENA}$ integrated along an LOS (θ, ϕ) is given as

$$J_{\rm ENA}(v_{\rm ENA}, t_{\rm ENA}, \theta, \phi) = \int_{l_{\rm TS}(t)}^{l_{\rm HP}(t)} \frac{1}{m_{\rm H}} f_p(\boldsymbol{r}, t, n, T) \times v n_{\rm H} \sigma_{\rm ex}(v_{\rm rel}) v_{\rm rel}(\boldsymbol{r}, v, t) dr. \quad (7)$$

Equation (7) is solved in the solar inertial frame, where $v = |\boldsymbol{v}_{\rm ENA} - \boldsymbol{u}_{\rm MHD}|$. The time of ENA observation, $t_{\rm ENA}$, accounts for the time for ENAs to travel from their plasma source to IBEX, such that $t = t_{\rm ENA} - l/v_{\rm ENA}$, where l is the LOS distance from IBEX to the ENA source. Equation (7) is also integrated over each IBEX-Hi ESA response function to obtain ENA fluxes comparable to its energy passbands (Funsten et al. 2009).

We analyze IBEX-Hi ENA observations taken over a full solar cycle (McComas et al. 2020). We compare to "ram" data (when IBEX's LOS is in the direction of Earth's motion) and "anti-ram" data (when IBEX's LOS is in the opposite direction of Earth's motion) corrected for ENA survival probabilities and the Compton–Getting effect when transforming to the solar inertial frame. IBEX ENA fluxes from both data and model results shown in Section 3 are statistically averaged over the 9 pixels nearest to the Voyager 2 trajectory, and the uncertainties are derived from the weighted standard deviation between the pixels.

Appendix C
χ^2 Minimization Analysis

We perform χ^2 minimization to determine the best-fit polytropic spectral indices for the HTS applied to time periods $T < 2014.75$ and >2014.75. First, we simulate ENA fluxes at 1 au at all IBEX-Hi energy passbands over the entire IBEX epoch for a range of polytropic heating indices. Then, we minimize the χ^2 statistic between IBEX data and our model, following similar methodology in Swaczyna et al. (2022),

$$\chi^2 = \sum_{i=1}^{N}\sum_{j=1}^{M}\frac{(J_o^{ij}-J_m^{ij})^2}{(\sigma_o^{ij})^2},$$
$$J_m^{ij} = J_m^{ij}(\gamma_{1,0},\,\gamma_{2,0}) + S^i + (\gamma_1-\gamma_{1,0}) \times\left[\frac{J_m^{ij}(\gamma_{1,0}+\delta_1,\,\gamma_{2,0}) - J_m^{ij}(\gamma_{1,0}-\delta_1,\,\gamma_{2,0})}{2\delta_1}\right] + (\gamma_2-\gamma_{2,0})\left[\frac{J_m^{ij}(\gamma_{1,0},\,\gamma_{2,0}+\delta_2) - J_m^{ij}(\gamma_{1,0},\,\gamma_{2,0}-\delta_2)}{2\delta_2}\right]. \quad (8)$$

Here J_o^{ij} is the observed ENA flux, J_m^{ij} is the model ENA flux, superscript i represents ESA passbands 2–6, and superscript j represents observation times at 1 au. Because we are comparing results equally weighted over 9 pixels, whose variation in space is assumed to be physically meaningful, the data uncertainties in the fits, σ_o^{ij}, are assumed to be the unweighted standard deviation over the 9 observation pixels. Here S^i represents the separate ENA source parameter as a function of ESA passband. The fit parameters γ_1 and γ_2 are the polytropic heating indices at the HTS for the two time periods, and δ_1 and δ_2 are the half-widths of the sampling windows. The model flux is estimated as a function of these indices using Taylor expansions around an initial guess $(\gamma_{1,0}, \gamma_{2,0}) = (2.2, 2.6)$, with derivatives estimated using finite differences.

We minimize Equation (8) using least-squares regression, requiring that the separate source parameters must be greater than or equal to zero. We perform two sets of minimizations, one assuming $\gamma_{\rm IHS} = 5/3$ and the other $\gamma_{\rm IHS} = 2$. The best-fit results for the polytropic indices are $\gamma_{1,2}(\gamma_{\rm IHS} = 5/3) = (2.35, 2.73)$ and $\gamma_{1,2}(\gamma_{\rm IHS} = 2) = (2.28, 2.67)$, and the separate sources as a function of ESA passband are $S^i(\gamma_{\rm IHS} = 5/3) = (25.6, 18.0, 7.9, 2.3, 0.0)$ and $S^i(\gamma_{\rm IHS} = 2) = (27.4, 18.7, 8.0, 2.4, 0.0)$ in differential flux units of number of ENAs/(cm^2 s sr keV)/(cm^2 s sr keV). Note that the minimization process yielded values of 0.0 for the ESA 6 separate source, effectively removing this as a fitting parameter and leading to underestimated uncertainties. Therefore, we perform the same minimizations again, but all parameters S^i are allowed to be negative, and we find uncertainties of $\sigma_{\gamma 1,2}(\gamma_{\rm IHS} = 5/3) = (0.09, 0.07)$, $\sigma_{\gamma 1,2}(\gamma_{\rm IHS} = 2) = (0.09, 0.07)$, $\sigma_S^i(\gamma_{\rm IHS} = 5/3) = (10.9, 6.6, 3.8, 1.9, 0.8)$, and $\sigma_S^i(\gamma_{\rm IHS} = 2) = (10.7, 6.7, 3.9, 2.1, 0.9)$. We therefore choose nominal values of the HTS polytropic heating indices and their uncertainties to be $\gamma_{1,2} = (2.31 \pm 0.09, 2.70 \pm 0.07)$. Finally, we note that testing our analysis using the heliosphere simulation results from Kim et al. (2017) yielded a smaller HTS heating index after 2014.75 of $\gamma_2(\gamma_{\rm IHS} = 5/3) = 2.49$ with uncertainty $\sigma_{\gamma 2}(\gamma_{\rm IHS} = 5/3) = 0.05$.

We note that the separate ENA source results shown in Figure 4(f) are computed by performing an independent χ^2 minimization between the model simulated with $\gamma_{\rm HTS1} = 2.3$ and $\gamma_{\rm HTS2} = 2.7$ and the data, yielding the separate ENA source values similar to those reported in this section. However, we use the larger uncertainties of (10.9, 6.7, 3.9, 2.1, 0.9) in Figure 4(f) performed by the analysis in this section.

ORCID iDs

E. J. Zirnstein https://orcid.org/0000-0001-7240-0618
T. K. Kim https://orcid.org/0000-0003-0764-9569
M. A. Dayeh https://orcid.org/0000-0001-9323-1200
J. S. Rankin https://orcid.org/0000-0002-8111-1444
D. J. McComas https://orcid.org/0000-0001-6160-1158
P. Swaczyna https://orcid.org/0000-0002-9033-0809

References

Baliukin, I. I., Izmodenov, V. V., & Alexashov, D. B. 2020, MNRAS, 499, 441
Baranov, V. B., & Malama, Y. G. 1993, JGR, 98, 15157
Burlaga, L. F., Ness, N. F., Berdichevsky, D. B., et al. 2022, ApJ, 932, 59
Bzowski, M., Sokół, J. M., Tokumaru, M., et al. 2013, in Cross-Calibration of Far UV Spectra of Solar System Objects and the Heliosphere, ed. E. Quémerais, M. Snow, & R.-M. Bonnet (New York: Springer), 67
Chalov, S. V., Fahr, H. J., & Izmodenov, V. V. 2003, JGRA, 108, 1266
Cummings, A. C., Stone, E. C., Richardson, J. D., et al. 2021, ApJ, 906, 126
Funsten, H. O., Allegrini, F., Bochsler, P., et al. 2009, SSRv, 146, 75
Fuselier, S. A., Galli, A., Richardson, J. D., et al. 2021, ApJL, 915, L26
Giacalone, J., Nakanotani, M., Zank, G. P., et al. 2021, ApJ, 911, 27
Gkioulidou, M., Opher, M., Kornbleuth, M., et al. 2022, ApJL, 931, L21
Izmodenov, V. V., Malama, Y. G., Ruderman, M. S., et al. 2009, SSRv, 146, 329
Karna, N., Hess Webber, S. A., & Pesnell, W. D. 2014, SoPh, 289, 3381
Kim, T. K., Pogorelov, N. V., & Burlaga, L. F. 2017, ApJL, 843, L32
Kim, T. K., Pogorelov, N. V., Zank, G. P., Elliott, H. A., & McComas, D. J. 2016, ApJ, 832, 72
Kornbleuth, M., Opher, M., Baliukin, I., et al. 2021, ApJ, 921, 164
Kumar, R., Zirnstein, E. J., & Spitkovsky, A. 2018, ApJ, 860, 156
Lallement, R., Quémerais, E., Koutroumpa, D., et al. 2010, in AIP Conf. Proc. 1216, Twelfth International Solar Wind Conference, ed. M. Maksimovic et al. (Melville, NY: AIP), 555
Lee, M. A., Fahr, H. J., Kucharek, H., et al. 2009, SSRv, 146, 275
McComas, D. J., Allegrini, F., Bochsler, P., et al. 2009, Sci, 326, 959
McComas, D. J., Bzowski, M., Dayeh, M. A., et al. 2020, ApJS, 248, 26
McComas, D. J., Bzowski, M., Fuselier, S. A., et al. 2015, ApJS, 220, 22
McComas, D. J., Christian, E. R., Schwadron, N. A., et al. 2018a, SSRv, 214, 116
McComas, D. J., Dayeh, M. A., Funsten, H. O., et al. 2018b, ApJL, 856, L10
McComas, D. J., Ebert, R. W., Elliott, H. A., et al. 2008, GeoRL, 35, L18103
McComas, D. J., Shrestha, B. L., Swaczyna, P., et al. 2022, ApJ, 934, 147
McComas, D. J., Swaczyna, P., Szalay, J. R., et al. 2021, ApJS, 254, 19
Mostafavi, P., Zank, G. P., Zirnstein, E. J., & McComas, D. J. 2019, ApJL, 878, L24
Opher, M., Prested, C., McComas, D. J., Schwadron, N. A., & Drake, J. F. 2013, ApJL, 776, L32
Parker, E. N. 1961, ApJ, 134, 20
Pauls, H. L., Zank, G. P., & Williams, L. L. 1995, JGR, 100, 21595
Pogorelov, N., Borovikov, S., Heerikhuisen, J., et al. 2014, in Proc. 2014 Annual Conf. on Extreme Science and Engineering Discovery Environment, ed. S. Lathrop & J. Alameda (New York: Association for Computing Machinery), 1
Pogorelov, N. V., Suess, S. T., Borovikov, S. N., et al. 2013, ApJ, 772, 2
Pogorelov, N. V., Zank, G. P., & Ogino, T. 2006, ApJ, 644, 1299
Richardson, J. D., Cummings, A. C., Burlaga, L. F., et al. 2021, ApJL, 919, L28
Richardson, J. D., Kasper, J. C., Wang, C., Belcher, J. W., & Lazarus, A. J. 2008, Natur, 454, 63
Richardson, J. D., Wang, C., Liu, Y. D., et al. 2017, ApJ, 834, 190
Schwadron, N. A., Allegrini, F., Bzowski, M., et al. 2018, ApJS, 239, 1
Schwadron, N. A., & McComas, D. J. 2013, ApJ, 764, 92

Schwadron, N. A., & McComas, D. J. 2019, ApJ, 887, 247
Sokół, J. M., McComas, D. J., Bzowski, M., & Tokumaru, M. 2020, ApJ, 897, 179
Swaczyna, P., Kubiak, M. A., Bzowski, M., et al. 2022, ApJS, 259, 42
Swaczyna, P., McComas, D. J., Zirnstein, E. J., et al. 2020, ApJ, 903, 48
Tokumaru, M., Fujiki, K., Kojima, M., & Iwai, K. 2021, ApJ, 922, 73
Wu, P., Winske, D., Gary, S. P., Schwadron, N. A., & Lee, M. A. 2009, JGRA, 114, A08103
Yang, Z., Liu, Y. D., Richardson, J. D., et al. 2015, ApJ, 809, 28
Zank, G. P., Adhikari, L., Zhao, L.-L., et al. 2018, ApJ, 869, 23
Zank, G. P., Pauls, H. L., Cairns, I. H., & Webb, G. M. 1996, JGR, 101, 457
Zirnstein, E. J., Dayeh, M. A., Heerikhuisen, J., McComas, D. J., & Swaczyna, P. 2021a, ApJS, 252, 26
Zirnstein, E. J., Heerikhuisen, J., Funsten, H. O., et al. 2016, ApJL, 818, L18
Zirnstein, E. J., Heerikhuisen, J., Zank, G. P., et al. 2014, ApJ, 783, 129
Zirnstein, E. J., Heerikhuisen, J., Zank, G. P., et al. 2017, ApJ, 836, 238
Zirnstein, E. J., Kumar, R., Bandyopadhyay, R., et al. 2021b, ApJL, 916, L21
Zirnstein, E. J., Kumar, R., Heerikhuisen, J., McComas, D. J., & Galli, A. 2018a, ApJ, 860, 170
Zirnstein, E. J., McComas, D. J., Kumar, R., et al. 2018b, PhRvL, 121, 075102
Zirnstein, E. J., McComas, D. J., Schwadron, N. A., et al. 2019, ApJ, 876, 92
Zirnstein, E. J., Möbius, E., Zhang, M., et al. 2022, SSRv, 218, 28